Scatterometer Beam Balancing Using Open-Ocean Backscatter Measurements

MICHAEL H. FREILICH AND HONGBO QI

College of Oceanic and Atmospheric Sciences, Oregon State University, Corvallis, Oregon

R. SCOTT DUNBAR

Jet Propulsion Laboratory, California Institute of Technology, Pasadena, California

(Manuscript received 11 July 1996, in final form 6 April 1998)

ABSTRACT

Calculation of vector winds from spaceborne fan-beam scatterometers requires that backscatter measurements from different antennas be relatively calibrated to high accuracy. A method is developed to perform postlaunch antenna calibration using global mean ocean backscatter measurements in conjunction with estimates of the statistical distribution of near-surface wind velocity and the model function relating backscatter to winds. Substantial analytic simplifications result from assuming that the wind speed and azimuth distributions are separable and that the upwind–downwind asymmetry term in the model function is small. The analytic model allows quantitative examination of the sensitivity of the technique to errors in the approximate wind distributions and empirical model function. The approach and its assumptions are tested using 13 months of *ERS-1* backscatter data, surface wind estimates from two operational weather analyses, and three empirical C-band model functions. It is shown that the *ERS-1* antennas are relatively calibrated to within 0.2 dB, which is consistent with other published results obtained using ground receiving stations and Amazon forest data. The results are nearly insensitive to realistic errors in the estimated wind velocity distributions and model function. Analysis suggests that the ocean antenna calibration technique should be accurate to about 0.2 dB using as little as 3 weeks of scatterometer data.

1. Introduction

Calculation of accurate vector winds from scatterometer data requires multiple backscatter (σ_o) measurements and knowledge of the model function relating σ_o to viewing geometry and environmental conditions (see Naderi et al. 1991 for a review of scatterometry). Fan-beam scatterometers acquire the collocated σ_o measurements employing several antennas that sequentially image the same earth locations as the satellite travels in its orbit. A single model function is typically used in ground-based processing, and thus systematic differences in σ_o measurements from different antennas can lead to deterministic errors in the calculated winds. Absolute σ_o calibration errors common to all antennas can be accommodated by tailoring the model function to the particular instrument. However, the use of a single model function requires that the σ_o measurements from all antennas be relatively calibrated to high accuracy. This interantenna calibration process will be called ''beam balancing'' hereafter.

Several different beam-balancing approaches were used for Seasat SASS and the *ERS-1/2* scatterometers. The antennas are typically calibrated prior to launch using standard techniques and antenna ranges. However, prelaunch calibration of scatterometer fan-beam antennas is notoriously difficult, and launch and deployment effects can modify the effective in-orbit antenna beam patterns.

The *ERS-1/2* AMI programs used a small number of calibrated ground receivers to precisely measure the received power from each beam as the spacecraft passes overhead (Lecomte and Attema 1993). However, only a few such stations can be deployed, greatly constraining the number of incidence angles that can be examined on each pass. In addition, the relatively infrequent satellite overpasses do not allow statistically significant results to be obtained rapidly.

Several studies have developed beam-balancing techniques based on analyzing backscatter measurements from land areas believed to have approximately homogeneous and isotropic scattering characteristics (Birrer et al. 1982; Kennett and Li 1989; Lecomte and Attema 1993; Long and Skouson 1996). Although issues

Corresponding author address: Michael H. Freilich, College of Oceanic and Atmospheric Sciences, Oregon State University, 104 Ocean Admin. Building, Corvallis, OR 97331-5503.
E-mail: mhf@oce.orst.edu

associated with homogeneity, the precise degree of isotropy, and diurnal variations in the properties of the scattering regions continue to be investigated, the primary initial beam-balancing analyses for SASS and *ERS-1/2* were based on spaceborne scatterometer data acquired over the Amazon forest region (Birrer et al. 1982; Lecomte and Attema 1993).

This paper examines the possibility that open-ocean backscatter measurements can be used to perform quantitative beam balancing for spaceborne fan-beam scatterometers. The large extent of the global oceans provides a large number of measurements in short time periods, and the dynamic range of the ocean backscatter data is precisely what is required for vector wind calculations. However, the ocean is not an isotropic scatterer; indeed, it is the very anisotropy of backscatter with respect to azimuth angle that allows scatterometers to be used to infer wind direction as well as speed. Beam balancing using open-ocean σ_o measurements thus requires additional information, typically in the form of auxiliary measurements of the wind field or a priori assumptions about the statistical distributions of wind speeds and relative directions imaged by each of the antennas.

Stoffelen and Anderson (1995; see also Stoffelen 1999) independently used collocated *ERS-1* ocean backscatter measurements and wind speed and direction information from operational surface wind analyses to perform relative beam balancing. In their approach, the full ensemble of collocated measurements in wind speed bands (defined by the surface analyses) and incidence angle (determined from the scatterometer data) was randomly subsampled to achieve a uniform directional distribution, thus simplifying the analytic development (see sections 2 and 4).

The present study develops and tests an approach that utilizes approximate knowledge of the global distributions of wind speed and direction derived from operational numerical weather prediction surface analyses, as well as similarly approximate knowledge of the general features of the model function relating backscatter to vector winds. This approach differs from that of Stoffelen and Anderson in that operational surface analyses interpolated to the scatterometer measurement locations are used only to construct approximate wind speed and relative azimuth distributions. The primary goal of this study is to estimate the accuracy with which beam balancing can be achieved based on limited quantities of open-ocean σ_o measurements in the earliest stages of satellite missions. The method is tested using data from the *ERS-1* AMI instrument.

The analytic basis for beam balancing using open-ocean σ_o measurements is developed in section 2. In section 3, 13 months of twice-daily European Centre for Medium Range Weather Forecasts (ECMWF) and U.S. National Meteorological Center [(NMC), now known as the National Centers for Environmental Prediction (NCEP)] operational surface wind analyses are interpolated to the space–time locations of *ERS-1* σ_o measurements in order to provide estimates of the distributions of wind speed and relative azimuth. The dependence of the antenna calibration error estimates on the model function used for the analysis is investigated in section 4. In section 5, the 13-month dataset is used to obtain antenna calibration error estimates for the *ERS-1* fore and mid beams (relative to the aft beam) using three different empirical C-band model functions. Section 6 empirically examines the dependence of relative calibration error estimates on the averaging period used to construct the sample mean backscatters and wind velocity distributions. Discussion and conclusions follow in section 7.

2. Analytic development

The beam-balancing technique presented here can identify and correct a class of time-independent relative calibration differences between scatterometer antennas. The technique uses open-ocean σ_o measurements, in conjunction with auxiliary information on the statistics of wind velocity and the approximate dependence of the model function on incidence angle (θ), wind speed (s), and relative azimuth (χ), defined to be the angle in the horizontal plane between the projection of the radar beam and the direction from which the wind is blowing. Although exact knowledge of s, χ, and the model function for each σ_o measurement would allow the beam-balancing problem to be solved trivially, the auxiliary information is generally imperfectly known.

The technique developed here utilizes only sample mean σ_o data and approximations to the global distributions of s and χ imaged by each scatterometer antenna at each incidence angle, rather than knowledge of the precise wind velocity associated with each σ_o measurement. It is thus insensitive to realistic errors in individual wind velocity estimates obtained from operational numerical weather prediction system surface wind analyses. Similarly, the empirical model function is often imperfectly known. It is shown in section 5 that the technique is robust and demonstrates little sensitivity to model function errors since different proposed model functions yield similar beam balance results.

The relationship between the ''true'' backscatter cross section (σ_o) and near-surface environmental conditions is given by

$$\sigma_o \equiv f(s, \chi, \ldots; \theta), \tag{1}$$

where $f(s, \chi, \ldots; \theta)$ is the true model function and ''. . .'' indicates the effects of nonwind geophysical conditions such as long waves, atmospheric stratification, sea surface temperature, etc. Under most conditions these subsidiary geophysical effects are small, and they are not further considered in this development.

The actual backscatter measurements $\hat{\sigma}_o$ can be contaminated by both calibration errors and random noise, so

$$\hat{\sigma}_o(s, \chi; \theta, b) \equiv R(\theta, b)\sigma_o(s, \chi; \theta) + e(\sigma_o; \theta, b), \quad (2)$$

where b denotes a specific antenna beam, $R(\theta, b)$ represents time-invariant, deterministic, multiplicative calibration errors for beam b at incidence angle θ, and e is a random variable representing instrumental and communication noise. By convention, $b = 1$ corresponds to the fore beam for a given swath and b is incremented for every additional antenna beam imaging the swath at different azimuths and/or polarizations. For the *ERS-1/2* AMI instruments, $1 \leq b \leq 3$, while for the NSCAT scatterometer instrument, $1 \leq b \leq 4$ for each of the two swaths (NSCAT acquired vertically and horizontally polarized measurements from two separate antennas at the mid-beam azimuth). The random variable e is assumed to be normally distributed with zero mean. All backscatter cross sections are in natural (not decibels) units in this derivation, and thus the variance of e is a function of σ_o, θ, and b.

The sample mean backscatter measured by antenna b at θ is given by

$$\langle \hat{\sigma}_o(\theta, b) \rangle = \int_{s=0}^{\infty} \int_{\chi=0}^{2\pi} p(s, \chi; \theta, b)\hat{\sigma}_o(\theta, b)\, d\chi\, ds, \quad (3)$$

where $p(s, \chi; \theta, b)$ is the sample joint probability density function (PDF) of wind speed and relative azimuth imaged by the antenna. In practice, $p(s, \chi; \theta, b)$ is approximated by the normalized two-dimensional histogram of measured wind velocities, and the integrals over s and χ are replaced by sums over the sample populations. However, p and the integral notation will be used below for clarity.

Significant analytic simplifications result if it can be assumed that s and χ are independent, so that

$$p(s, \chi; \theta, b) = p_s(s; \theta, b)p_\chi(\chi; \theta, b), \quad (4)$$

and that the model function f can also be approximated as the truncated Fourier series

$$f(s, \chi; \theta) = \sum_{n=0}^{M} A_n(s; \theta) \cos(n\chi), \quad (5)$$

where M is a small integer, typically $M = 2$. Then (3) becomes

$$\langle \hat{\sigma}_o(\theta, b) \rangle = R(\theta, b) \sum_{n=0}^{M} \left[\int_{s=0}^{\infty} A_n(s; \theta)p_s(s; \theta, b)\, ds \times \int_{\chi=0}^{2\pi} p_\chi(\chi; \theta, b) \cos(n\chi)\, d\chi \right] + \int_0^{\infty} \int_0^{2\pi} p_s p_\chi e(\sigma_o; \theta, b)\, ds\, d\chi. \quad (6)$$

The validity of the approximation (4) is discussed in sections 3 and 4.

The overall sample mean error term in (6) will be negligible if the individual random errors are small or if sufficient measurements exist for each true value of σ_o for each beam. If the random error term is neglected, each element of the remaining sum on the right-hand side of (6) is a product of the mean model function coefficient (averaged with respect to the wind speed distribution observed by antenna b at incidence angle θ) and the weighted mean value of $\cos(n\chi)$ (averaged with respect to the observed azimuthal distribution).

Relative beam balancing requires choice of one beam to be the ''standard,'' denoted in the following as $\hat{b}$. If sample mean backscatters are calculated from both the standard and another antenna ''b'' at identical incidence angles, (6) can be used to calculate the relative calibration:

$$F(\theta, b, \hat{b}) = \frac{R(\theta, b)}{R(\theta, \hat{b})}, = \left(\frac{\langle \hat{\sigma}_o(\theta, b) \rangle}{\langle \hat{\sigma}_o(\theta, \hat{b}) \rangle} \right) \frac{\sum_n^M \left[\int_0^{\infty} A_n(s; \theta)p_s(s; \theta, \hat{b})\, ds \int_0^{2\pi} p_\chi(\chi; \theta, \hat{b}) \cos(n\chi)\, d\chi \right]}{\sum_n^M \left[\int_0^{\infty} A_n(s; \theta)p_s(s; \theta, b)\, ds \int_0^{2\pi} p_\chi(\chi; \theta, b) \cos(n\chi)\, d\chi \right]}. \quad (7)$$

The relationship (7) clearly illustrates the roles played by the sample mean backscatter measurements, the model function [through the coefficients $A_n(s; \theta)$], and the (assumed independent) distributions of s and χ imaged by each of the antennas.

The notation can be simplified by defining

$$C_{n1}(\theta, b) \equiv \int_0^{\infty} A_n(s; \theta)p_s(s; \theta, b)\, ds, \quad (8a)$$

$$C_{n2}(\theta, b) \equiv \int_0^{2\pi} p_\chi(\chi; \theta, b) \cos(n\chi)\, d\chi, \quad (8b)$$

(note that $C_{02} = 1$) and

TABLE 1. Empirically determined scale factors used to reduce NMC 1000-mb wind velocity components to 10-m height.

	Atlantic			Pacific			Indian	
	−50°–−25°	−25°–25°	25°–50°	−50°–−25°	−25°–25°	25°–50°	−50°–−25°	−25°–25°
Scale factor	0.82	0.87	0.89	0.83	0.86	0.86	0.84	0.85

$$C_n \equiv C_{n1} C_{n2}. \tag{8c}$$

Truncating the model function Fourier series at $M = 2$, (7) becomes

$$F(\theta, b, \hat{b}) = \left(\frac{\langle \hat{\sigma}_o(\theta, b)\rangle}{\langle \hat{\sigma}_o(\theta, \hat{b})\rangle}\right)\frac{[C_0(\theta, \hat{b}) + C_1(\theta, \hat{b}) + C_2(\theta, \hat{b})]}{[C_0(\theta, b) + C_1(\theta, b) + C_2(\theta, b)]}. \tag{9}$$

3. Wind speed and direction distributions

This section examines the validity of the assumption (4) and determines approximate forms for $p_s(s;\ \theta,\ b)$ and $p_\chi(\chi;\ \theta,\ b)$, based on *ERS-1* data acquired during 1 June 1992–30 June 1993. Estimates of the observed wind velocities were derived by interpolating operational numerical weather prediction surface wind analyses to the space–time locations of *ERS-1* σ_o observations. Although the accuracies of the operational analyses are not well quantified and may vary with geographical location (particularly in the Southern Hemisphere, where ocean areas dominate and conventional surface measurements are virtually nonexistent), the operational products assimilate all relevant data and are thought to be highly constrained by observations. In comparison with some other beam-balancing and model function refinement approaches (e.g., Freilich and Dunbar 1993a,b; Stoffelen 1999), which rely on the accuracy of the individual NWP velocities, the present analysis uses the operational surface wind products to construct estimates of the relative wind velocity PDF imaged by each of the scatterometer antennas.

Both ECMWF and NMC operational surface wind analyses were used to estimate the surface winds imaged by the scatterometer antennas. The ECMWF data were obtained in the form of zonal (u) and meridional (v) 10-m component speeds. The twice-daily (0000 and 1200 UTC) analyses provided global wind velocity estimates on a 2.5° × 2.5° grid (Shaw et al. 1987; Lönnberg et al. 1992).

The NMC component speeds were similarly available twice-daily on the 2.5° global grid. However, the NMC components corresponded to 1000-mb rather than 10-m winds, and thus had to be transformed to 10-m estimates prior to merging with the ECMWF analyses. Freilich and Dunbar (1993a) multiplied the NMC wind speeds and velocity components by a global constant factor to reduce the 1000-mb estimates to 19.5-m height, based on a nonlinear fit of NMC and ECMWF global wind speed histograms for 1987. More detailed examination of the 1992–93 operational products used in the present study revealed geographical biases between the NMC and ECMWF surface wind analyses, suggesting that a single global-scale factor was inadequate. A histogram-matching analysis similar to that of Freilich and Dunbar (1993a) was thus performed in each of eight regions corresponding approximately to the North Pacific and Atlantic (25° to 50° latitude); the tropical Pacific, Atlantic, and Indian (−25° to 25° latitude); and the South Pacific, Atlantic, and Indian (−50° to −25° latitude) basins. In each region, the scale factor was chosen to minimize the normalized differences between those portions of the NMC and ECMWF wind speed histograms between 0.5 m s^{-1} and the 99.9 percentile point of the cumulative sample distributions. The resulting basin-dependent scale factors are given in Table 1.

Velocity components and speed magnitudes from the operational analyses were separately interpolated to the space–time locations of the σ_o measurement using trilinear interpolation (one time and two space dimensions). The interpolated components from the ECMWF and NMC analyses were then averaged to yield a single vector mean wind direction estimate, while the interpolated scalar speeds were averaged directly to yield a single speed estimate. Combining the analyses in this way cannot reduce errors common to both operational products. In addition, the relatively coarse temporal resolution of the twice-daily analyses can introduce interpolation errors, especially in mid- and high latitudes where temporal wind variability is large compared with the Tropics. Nonetheless, the use of two surface analyses has reduced random errors in related model function studies (Freilich and Dunbar 1993a).

The *ERS-1/2* AMI instruments operate in wind mode as vertically polarized, single-swath, three-look scatterometers with antenna beams oriented at nominal angles of 45°, 90°, and 135° relative to the satellite subtrack velocity (see Attema 1991 for detailed descriptions of the *ERS-1* AMI instrument and spacecraft.) The powerful transmitter used for the AMI results in high signal-to-noise ratios for the σ_o measurements, with reported normalized standard deviations of 4%–6% (although refined estimates taking into account the dominance of speckle noise suggest normalized standard deviations nearer to 15% for all wind conditions and swath locations; D. Offiler 1996, personal communication). The *ERS-1* spacecraft was maintained in a stable 35-day repeat orbit for the time period of this study. Although the spacecraft ground track repeated within ±1 km every 35 days (501 orbits), the orbit had a 3-day subcycle,

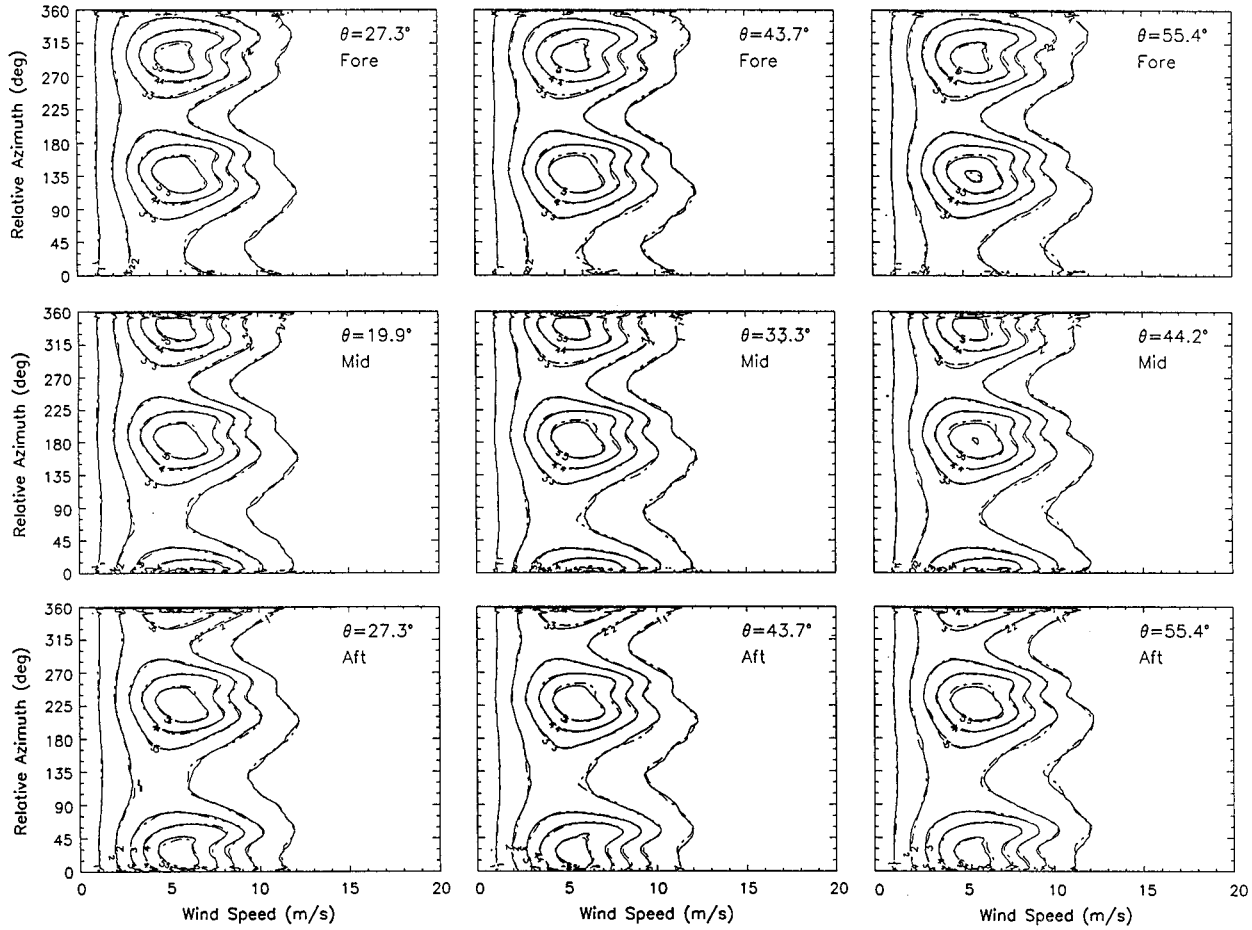

FIG. 1. Sample joint distributions $p(s, \chi; \theta, b)$ calculated from the full 13-month collocated operational surface wind analysis dataset. Distributions are shown for all three beams (fore, mid, and aft) and at selected incidence angles for each beam corresponding to inner-, mid–, and outer-swath locations. Solid contours: result from collocations based on the actual *ERS-1* measurement times. Dash–dot contours: based on collocations after adding an artificial offset of 36 h to the *ERS-1* measurement times.

leading to ''near repeats'' and substantial overlap of scatterometer swaths separated in time by 3 days.

Example joint distributions $p(s, \chi; \theta, b)$ are shown as solid contours in Fig. 1 for near-, mid-, and far-swath cells in each *ERS-1* beam. The sample distributions were derived by binning the interpolated speed (s) and relative wind azimuth (χ), creating two-dimensional histograms with 0.25 m s^{-1} and 2° resolution. Although only selected samples are shown in the figure, histograms corresponding to each of the 19 *ERS-1* cross-track σ_o cells were constructed for each beam. The similar shapes of the histograms in each row suggest that the measured relative wind velocity distributions did not vary appreciably with incidence angle.

Univariate distributions $p_s(s; \theta, b)$ and $p_\chi(\chi; \theta, b)$ calculated by integrating the joint distributions are shown in Figs. 2 and 3, respectively. The near-vertical contours again demonstrate that the long-term distributions are not sensitive functions of incidence angle. Integrating $p_s(s; \theta, b)$ and $p_\chi(\chi; \theta, b)$ over θ yields the one-dimensional s and χ distributions shown in Fig. 4. It is clear from Fig. 4a that each of the *ERS-1* antenna beams imaged nearly identical wind speed distributions over this 13-month period. However, the distinct curves in Fig. 4b demonstrate that although the periodic shapes of the azimuthal distributions are nearly identical for each beam, with peaks separated by about 180°, the curves from adjacent beams are offset by about 45°. Both the 45° directional offset (corresponding to the nominal 45° azimuthal separation of the three *ERS-1/2* beams) and the approximate 180° separation of the maxima in the individual curves are consistent with an underlying wind field dominated by the climatic zonal trades and westerlies and sampled by an instrument in near-polar orbit.

To illustrate the insensitivity of the long-term imaged speed and directional distributions to the synoptic details, the collocation of NWP-analyzed surface winds was also performed after adding an artificial 36-h offset to the *ERS-1* measurement times. The chosen 36-h offset is half of the 3-day *ERS-1* subcycle. Since the *ERS-1* geographical sampling nearly repeats every 3 days, a

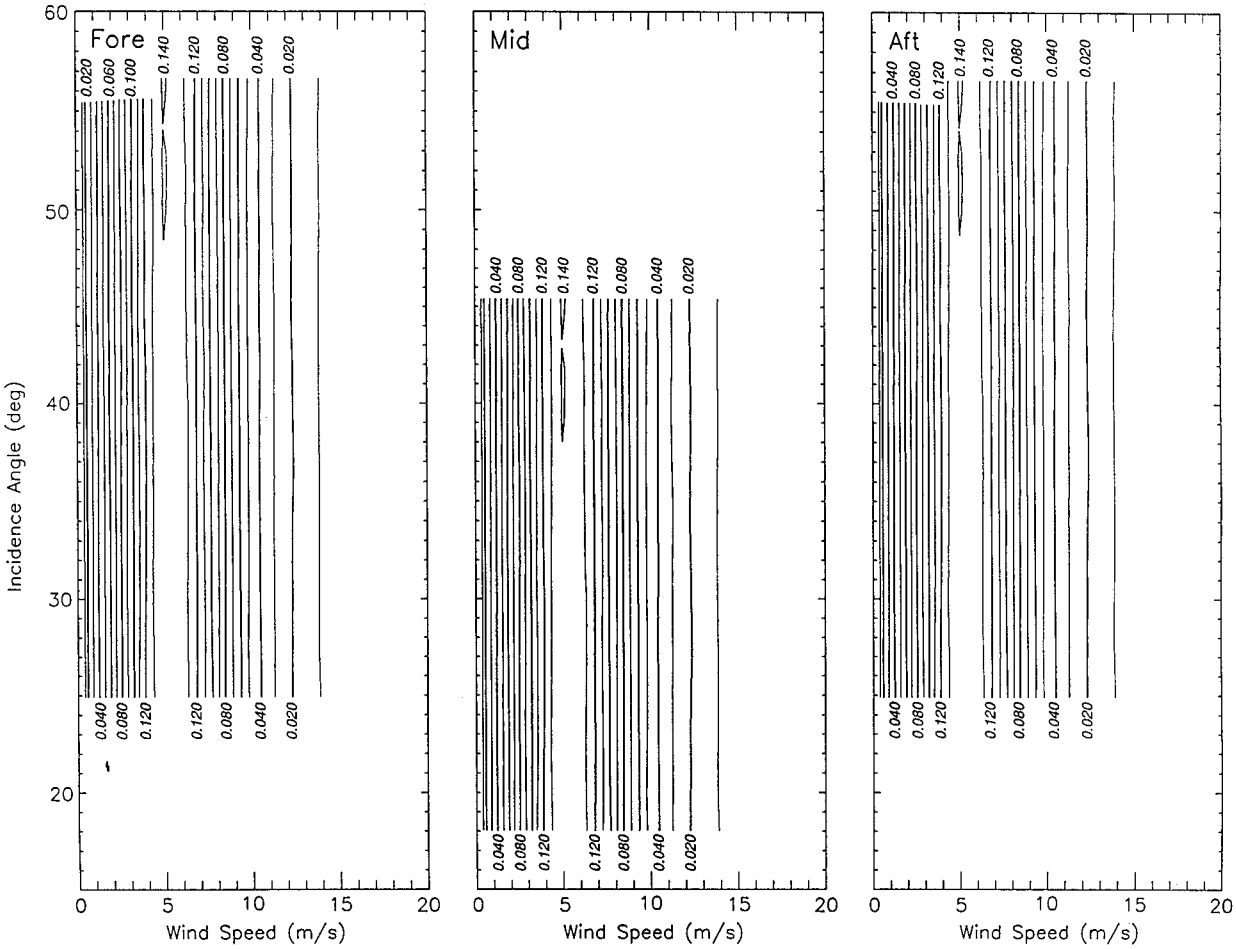

FIG. 2. Sample distributions $p_s(s;\ \theta)$ for each beam calculated from the full 13-month collocated dataset. Near-vertical contours indicate the near-insensitivity of p_s on θ.

36-h offset corresponds to synoptic features that were essentially unsampled in the original viewing geometry. As shown by the dashed contours in Fig. 1, the two simulations yield nearly identical two-dimensional distributions. Thus, at least for annual periods, the imaged speed and azimuthal distributions appear relatively insensitive to the details of the synoptic conditions and are determined primarily by the orbital and viewing geometry of the instrument and the synoptic statistics (rather than the detailed synoptic conditions) of the numerical weather prediction (NWP) models. Typical synoptic errors in the NWP fields therefore will not substantially degrade the empirical speed and directional distributions as long as the NWP analyses have generally realistic weather patterns and atmospheric evolution.

The accuracy of the separability assumption (4) is examined in Fig. 5. The solid contours in Fig. 5 are identical to the full two-dimensional distribution shown in Fig. 1, while the dashed contours result from the product of the individual one-dimensional distributions $p_s(s;\ \theta, b)$ and $p_\chi(\chi;\ \theta, b)$ as in (4). Although differences in the two distributions exist [especially at low wind speeds, where directions are more uniformly distributed than predicted by the approximate PDF (4)], the similarity of the two distributions for all beams and over the full range of cross-swath incidence angles suggests that the approximation (4) is at least qualitatively valid.

4. Model function dependence

The apparent beam and incidence angle independence of the wind speed distribution $p_s(s)$ allows straightforward analysis of the sensitivity of $F(\theta, b, \hat{b})$ to the model function's wind speed dependence. As shown in Fig. 4a, the long-term wind speed distribution at each incidence angle is highly concentrated near the midrange of the winds speeds (see also Wentz et al. 1984; Freilich and Dunbar 1993a; Freilich and Challenor 1994). The midrange of wind speeds will therefore contribute heavily to the overall integrals C_{n1}, although the wind speed dependence of the model function coefficients themselves will modify the influence of the wind speed distribution. Scatterometer model functions are empirically

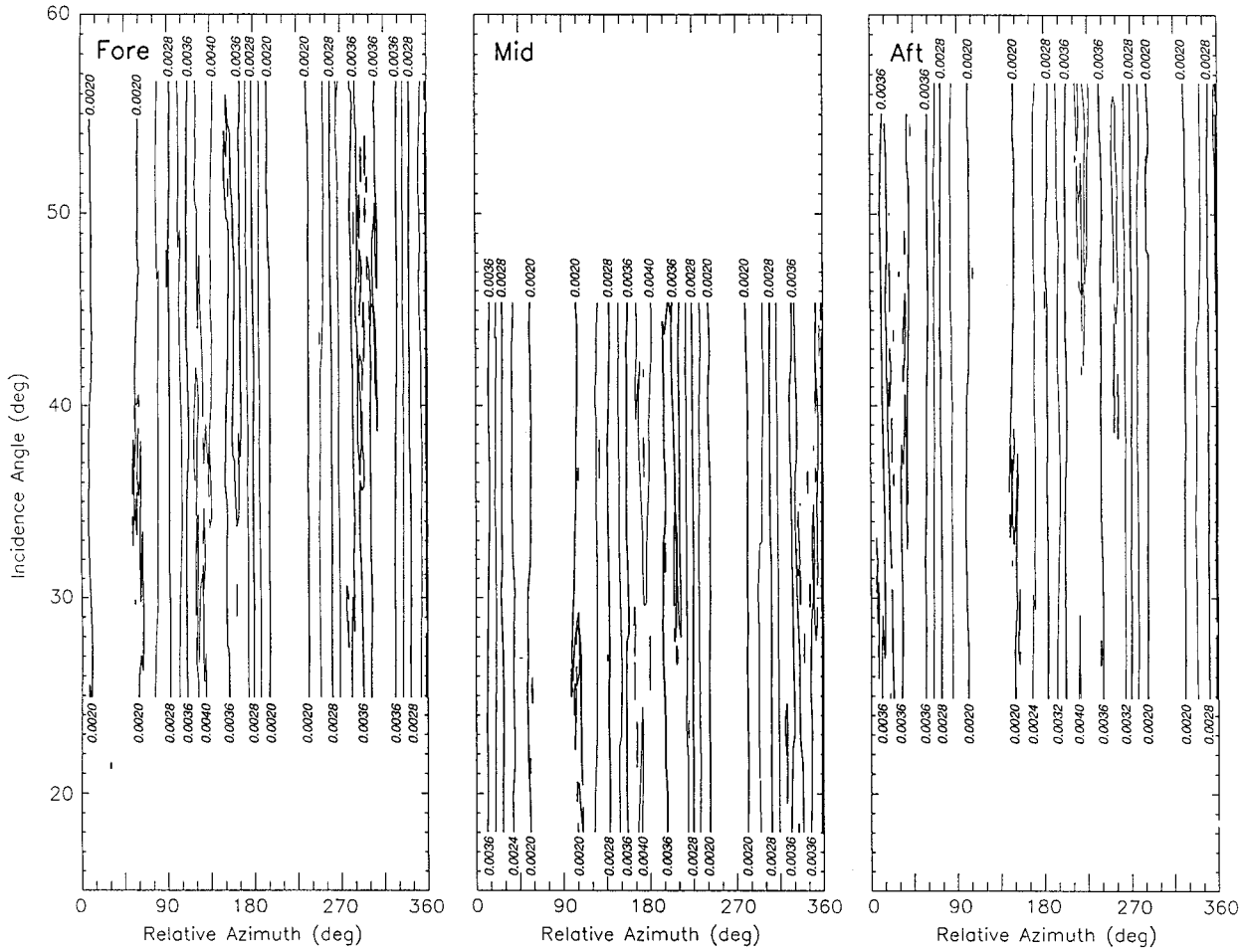

FIG. 3. As in Fig. 2 but for $p_\chi(\chi;\ \theta)$.

determined, and the coefficients A_n are least well known at both low and high wind speeds where accurate, extensive comparison measurements are lacking. Figures 6a,b illustrate the wind speed and incidence angle dependence of the full kernel $A_n(s;\ \theta)p_s(s)$, $(0 \le n \le 2)$ for the truncated azimuthal Fourier series approximation to the CMOD-4 model function (Offiler 1994; Stoffelen and Anderson 1995, 1997a–c). The shaded regions in the plots indicate the lower and upper wind speed regimes that cumulatively contribute less than 5% each to the value of C_{n1} at each θ. The wind speed region between about 3 and 13–14 m s^{-1} contributes 90% of the total values of $C_{01}(\theta)$ and $C_{21}(\theta)$. As CMOD-4 (and the other two model functions examined as well) yields reasonable wind velocities from *ERS-1/2* backscatter data over a wide range of wind speeds, it is unlikely that errors in the $A(n)$ coefficients at large and small wind speeds could be sufficiently large to influence the integrals $C_{01}(\theta)$ and $C_{21}(\theta)$ significantly (and thus to change the beam balance estimates). Beam balancing using the open-ocean data therefore does not require detailed knowledge of the model function at extreme wind speeds.

The lack of dependence of p_s on θ and b and the similar insensitivity of p_χ to changes in θ allow (9) to be further simplified and the model function dependence of F to be clarified. Since $C_{02} \equiv 1$ and p_s does not depend on b, $C_0 = C_{01}$ independent of b, and (9) can be rewritten

$$F(\theta, b, \hat{b}) = \left(\frac{\langle\hat{\sigma}_o(\theta, b)\rangle}{\langle\hat{\sigma}_o(\theta, \hat{b})\rangle}\right)\left[\frac{1 + G_1(\theta)C_{12}(\hat{b}) + G_2(\theta)C_{22}(\hat{b})}{1 + G_1(\theta)C_{12}(b) + G_2(\theta)C_{22}(b)}\right], \tag{10a}$$

where

$$G_n(\theta) = \frac{C_{n1}(\theta)}{C_{01}(\theta)} = \frac{C_{n1}(\theta)}{C_0(\theta)}. \tag{10b}$$

At each incidence angle, $G_n(\theta)$ is the speed-weighted mean A_n model function coefficient normalized by the

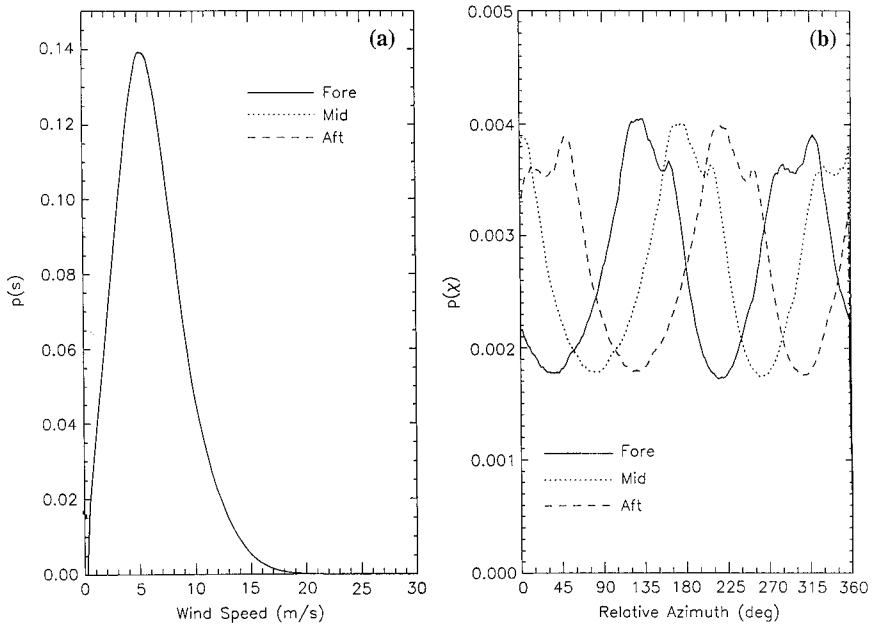

FIG. 4. (a) $p_s(s; b)$ for each beam. The fore-, mid-, and aft-beam distributions are indistinguishable. (b) $p_\chi(\chi, b)$ for each beam. Although the shapes of the distributions are nearly identical for each beam, the curves are offset by ~45°, which correspond to the azimuthal separations of the *ERS-1* beams.

(speed weighted) mean A_0 coefficient. As $\sigma_o \geq 0$ (in natural units), $A_n(s; \theta) \leq A_0(s; \theta)$ for $n \geq 1$; in practice, $|A_1(s; \theta)| \leq A_2(s; \theta) \leq A_0(s; \theta)$. Given the approximate 180° symmetry of p_χ, it is reasonable in (10) to neglect the terms $G_1(\theta)C_{12}(\hat{b})$ and $G_1(\theta)C_{12}(b)$, which is equivalent to assuming no upwind–downwind asymmetry in the model function. As shown in Fig. 7, $|C_1|/|C_0| = |G_1(\theta)C_{12}(b)|$ is small for the CMOD-4 model function for each of the three *ERS-1* beams. Neglect of any upwind–downwind asymmetry is similarly warranted for the Freilich and Dunbar (1993b) and the IFREMER (Bentamy et al. 1994) C-band model functions (not shown). (The normalized mean upwind–downwind asymmetry term in all three empirical model functions is small and negative for each beam when $\theta \lesssim 30°$, leading to the sharp dip in the $|C_1/C_0|$ curves for each beam as the ratio C_1/C_0 changes sign.) In addition, Fig. 7 demonstrates that $G_2(\theta) < 1$ and $C_2/C_0 < 1$ for all beams. Equation (10) can therefore be further simplified as

$$F(\theta, b, \hat{b}) = \left(\frac{\langle\hat{\sigma}_o(\theta, b)\rangle}{\langle\hat{\sigma}_o(\theta, \hat{b})\rangle}\right)\left[\frac{1 + G_2(\theta)C_{22}(\hat{b})}{1 + G_2(\theta)C_{22}(b)}\right]. \quad (11)$$

The fractional sensitivity of F to the model function estimates of G_2 is given by

$$\frac{1}{F(\theta, b, \hat{b})}\frac{\partial F(\theta, b, \hat{b})}{\partial G_2(\theta)} = \frac{C_{22}(\hat{b}) - C_{22}(b)}{(1 + G_2(\theta)C_{22}(\hat{b}))(1 + G_2(\theta)C_{22}(b))} \quad (12)$$

and shown in Fig. 8 for all three empirical C-band model functions.

The proposed open-ocean scatterometer beam-balancing technique thus does not require knowledge of the (small) upwind–downwind asymmetry model function term $A_1(s; \theta)$. Similarly, small uncertainties in the upwind–crosswind modulation term $A_2(s; \theta)$ and the directional distribution $p_\chi(\chi; \theta, b)$ will not result in large quantitative errors in the relative antenna gain correction estimates.

5. ERS-1 results

The 13-month (1 June 1992–30 June 1993) dataset was used to examine the relative beam balancing of the *ERS-1* AMI scatterometer instrument. The aft beam was taken as the standard (i.e., $\hat{b} = 3$). ESA's initial low-level processing of the *ERS-1* data results in very narrow distributions of θ for each antenna for each of the 19 cross-track σ_o cells in the *ERS-1* swath. It was therefore reasonable to calculate $\langle\hat{\sigma}_o(\theta, b)\rangle$ and the wind speed and direction distributions at the natural incidence angles for each beam, rather than at arbitrary regularly spaced incidence angles. As the fore- and aft-beam azimuths are symmetric with respect to the cross-track direction, the natural incidence angles are nearly identical for these two beams and the ratios indicated in (10)–(11) were calculated directly. The midbeam incidence angles ranged from 18° to 47° (as compared with 25°–59° for the fore and aft beams). The analysis for the midbeam was therefore restricted to the θ region of

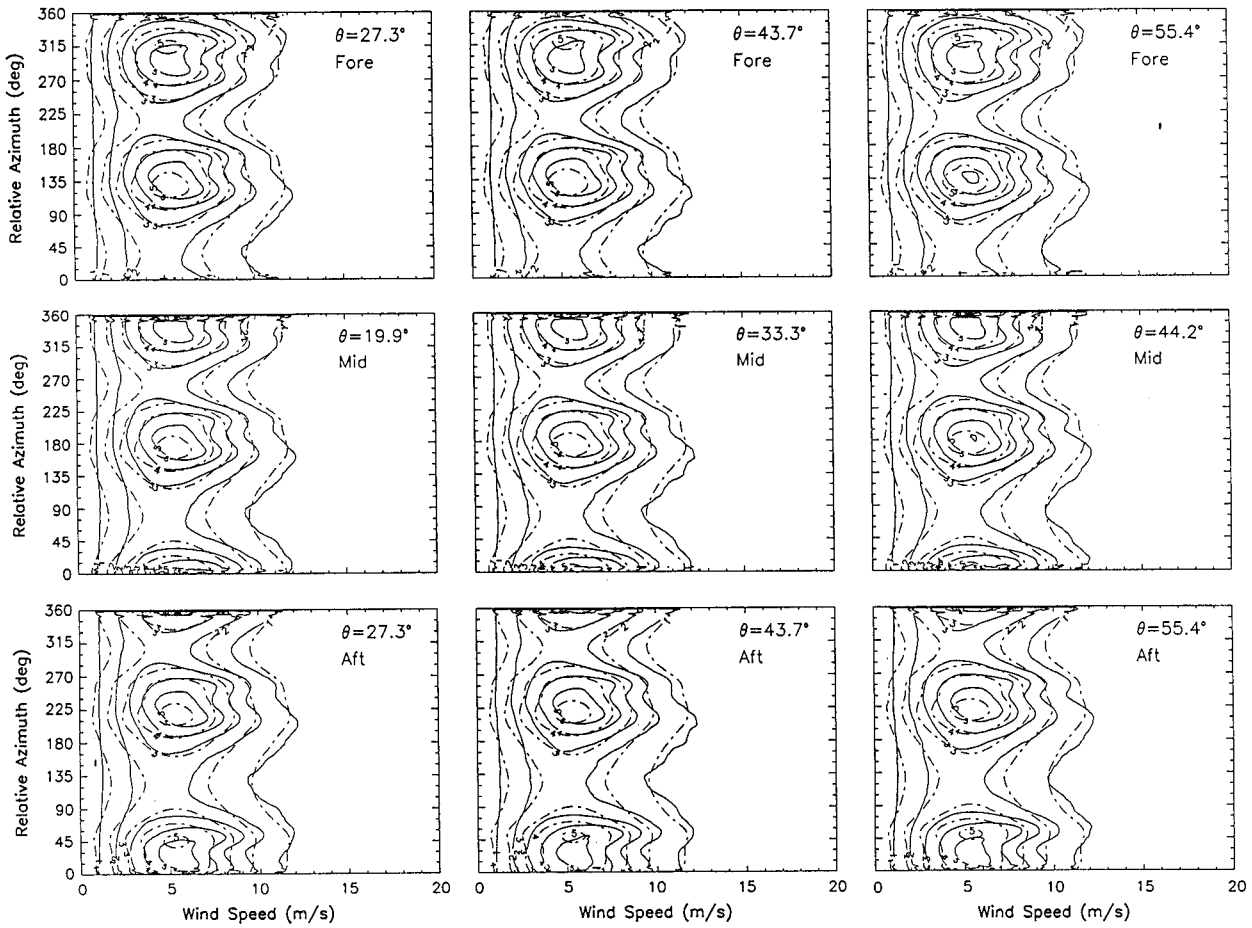

FIG. 5. Joint distributions $p(s, \chi; \theta, b)$ as in Fig. 1. Solid contours are identical to those in Fig. 1. Dash–dot contours denote the product $p_s(s)p_\chi(\chi, b)$ of the univariate distributions shown in Fig. 4.

overlap with the fore and aft beams, and quantities calculated at the natural incidence angles of the reference aft beam were interpolated to the natural incidence angles of the mid beam using cubic splines.

Results are shown for several different approximate expressions for $F(\theta, b, \hat{b})$ and all three C-band model functions in Figs. 9 and 10 for the mid and fore beams, respectively. All calculations used the single wind speed distribution shown in Fig. 4a (independent of θ and b) and the beam-dependent, θ-independent χ distributions from Fig. 4b. Multiple model functions were used to demonstrate the sensitivity of the relative gain correction estimates to realistic uncertainties in the model functions. In each of the figures, the unlabeled heavy lines correspond to solutions of the ''full'' expression (10), while unlabeled light lines are calculated assuming $A_1(s; \theta) = C_1(\theta, b) = 0$ [as in (11)].

The labeled lines result from setting $C_1 = C_2 = 0$ for each antenna beam, so that $F = (\langle\hat{\sigma}_o(\theta, b)\rangle / \langle\hat{\sigma}_o(\theta, \hat{b})\rangle)$. Setting $C_1 = C_2 = 0$ is consistent with the Wentz et al.'s (1984) assumption of a uniform azimuthal distribution for each antenna [$p_\chi(\chi; \theta, b) = (2\pi)^{-1}$]; however, Figs. 1–4 and the discussion of section 3 suggest that this is not a valid assumption.

The relative calibration estimates for the mid beam (with respect to the aft beam) are shown in Fig. 9. [Perfectly balanced beams would result in a horizontal line corresponding to a ratio of 0 dB or $F(\theta, b, \hat{b}) = 1$ in natural units.] For each model function, the unlabeled heavy and light lines are within about 0.01 dB of each other over the full θ range, demonstrating that both (10) and (11) yield quantitatively similar results. Each of the model functions yields small negative (in decibels) gain error estimates for the mid beam, corresponding to $F(\theta, 2, 3) \lesssim 1$. The Freilich–Dunbar and IFREMER model functions yield midbeam gain error estimates that differ from each other by less than 0.05 dB. The CMOD-4 model function results are similar to those of the other model functions at high incidence angles but diverge somewhat for $\theta < 40°$, resulting in a larger beam imbalance estimate. The estimated gain errors from all three model functions never differ by more than 0.11 dB over the full incidence angle range. The analysis

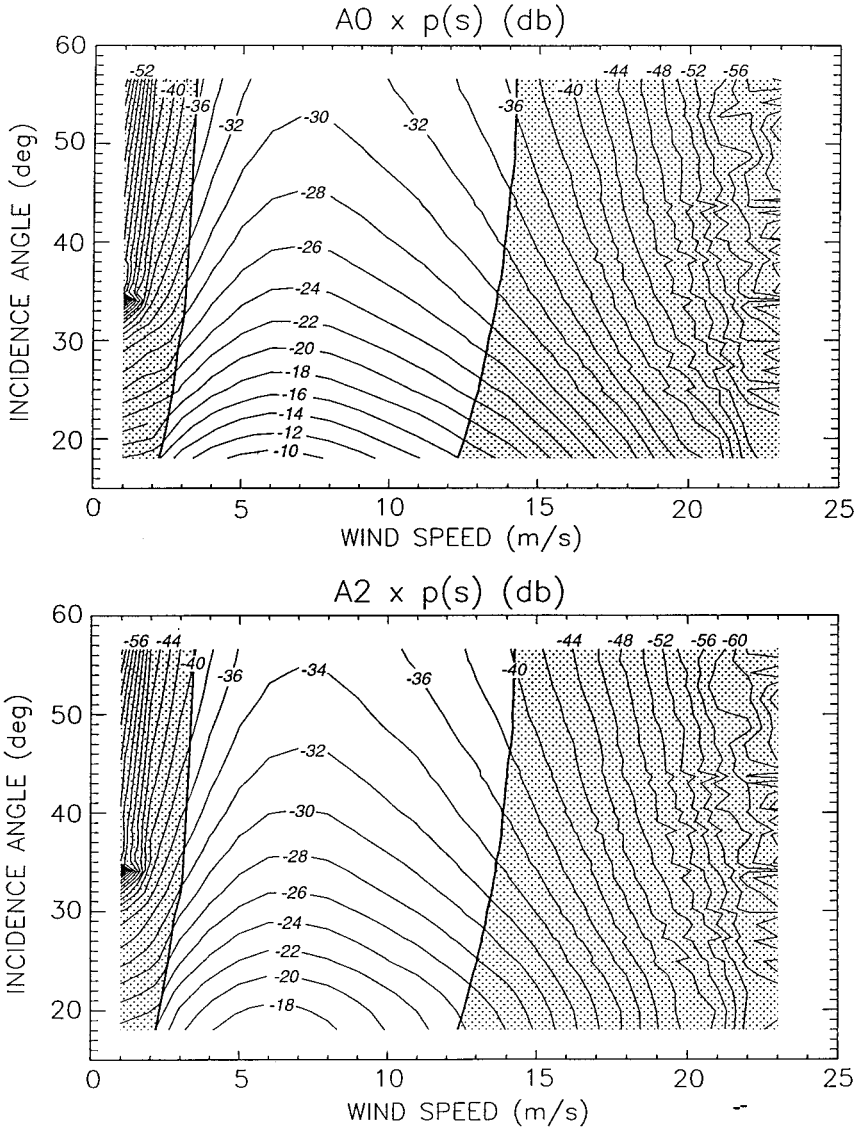

FIG. 6. (a) Contours of $A_0(s, \theta)p(s)$ for the CMOD-4 empirical C-band model function. Heavy solid lines denote the 5% and 95% cumulative percentage points of the product at each θ. Shaded areas thus each contribute less than 5% to the total integral at each θ. (b) As in (a) but for $A_2(s, \theta)p(s)$.

thus suggests that the mid and aft beams are balanced to $\ll$0.2 dB.

Although (10) and (11) yield small negative (in decibels) gain error estimates, use of only the C_0 mean model function coefficient results in an error estimate that is somewhat larger in magnitude and positive (in decibels) for all three model functions, with a definite trend toward increasing gain error with increasing incidence angle. The midbeam gain errors estimated by setting $C_1 = C_2 = 0$ for all three model functions are virtually identical, demonstrating that the weighted mean A_0 model function coefficients are quantitatively similar for all three model functions. However, the manifest inaccuracy of the assumption $C_2 = 0$ and the qualitative differences between these estimates of $F(\theta, 2, 3)$ and those obtained from (10) and (11) indicate that F cannot be estimated merely by calculating the mean backscatter ratios.

Figure 10 shows that the fore-beam relative gain error is greater than unity and larger in magnitude than the midbeam value. As was the case with the midbeam calculations, neglect of C_1 has little effect on the estimated fore-beam errors for all three model functions, the Freilich–Dunbar and IFREMER models agree most closely, gain error estimates from all three model functions are always within 0.07 dB, and the CMOD-4 estimates us-

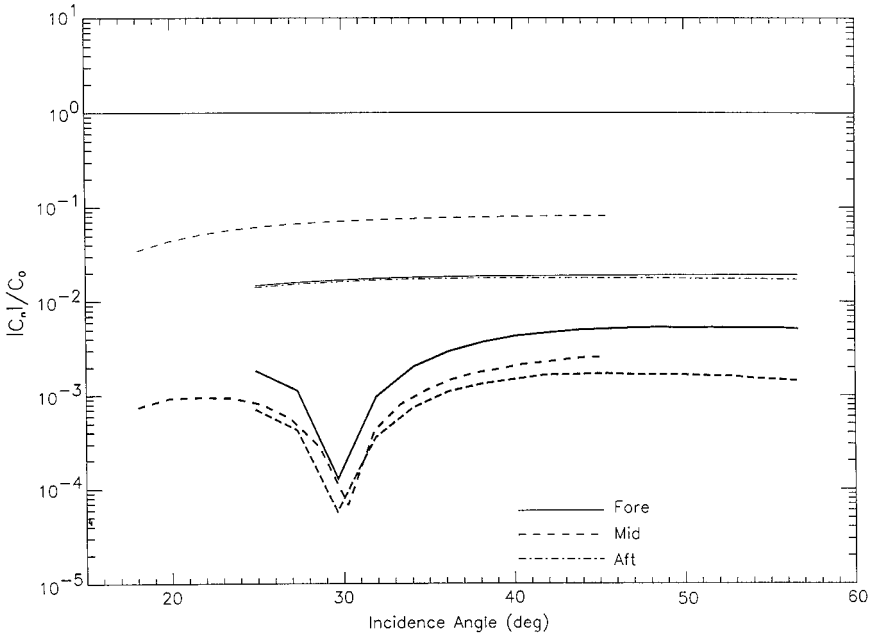

FIG. 7. $|C_n|/C_0$ vs θ for the CMOD-4 model function and for each *ERS-1* beam. Heavy lines: $|C_1|/C_0$; light lines: C_2/C_0.

ing (10) or (11) are larger in magnitude and diverge slightly from those of the other model functions at low incidence angles.

6. Variability of *F* with averaging period

The analyses of sections 3–5 used sample quantities calculated from a dataset covering 1 June 1992–30 June 1993. The large number of $\hat{\sigma}_o$ measurements and the large range of synoptic conditions encountered during this 13-month time span provided extremely accurate $\langle\hat{\sigma}_o\rangle$ and wind velocity distribution estimates. Similar results based on temporally extensive datasets will contribute significantly to the production of recalibrated, reprocessed scatterometer datasets one year or more after instrument turn-on. However, the scatterometer beams must be balanced prior to initial postlaunch model function refinement and geophysical validation analyses, and thus initial calibration of the antenna gain patterns must be accomplished relatively soon after launch. This section examines the variability of antenna gain error estimates as a function of the averaging period used in the calculation of $\langle\hat{\sigma}_o\rangle$ and the construction of sample wind velocity distributions.

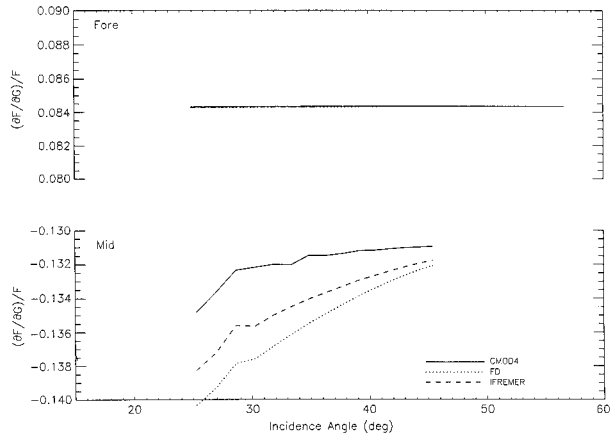

FIG. 8. Normalized sensitivity $(\partial G/\partial F)/F$ vs θ [cf. (12)] for the fore and mid beams relative to the aft beam for each model function.

The 56-week dataset used in sections 3–5 formed the basis for this time-dependent analysis as well. The dataset was divided into nonoverlapping segments, each of *k*-weeks duration, such that the *i*th segment corresponded to weeks $(i-1)k$ to ik. Operation of the *ERS-1* AMI in SAR mode (and associated transitions to and from scatterometer mode) led to noticeable quantities of missing ocean backscatter measurements. The calculations presented below thus represent realistic sample statistics. The detailed quantitative results would be expected to vary slightly if the analyses were performed on data acquired over a different time period.

Sample mean quantities calculated from segment *i* with segment length *k* are denoted by the subscript (i,k) (e.g., $\langle\hat{\sigma}_o(\theta, b)\rangle_{(i,k)}$). The sample joint distribution $p_{(i,k)}(s,\chi;\ \theta,\ b)$ was calculated for each segment and integrated to produce $p_{s,(i,k)}(s;\ \theta,\ b)$ and $p_{\chi,(i,k)}(\chi;\ \theta,\ b)$ as in section 3. Anticipating that the sample distributions based on short data segments would exhibit greater θ and b dependence than did the 56-week ''climatological'' distributions, general form (13) [equivalent to (9) with $C_{1,(\theta,b)} = C_{1,(\theta,\hat{b})} = 0$] was used to calculate the segment relative gain error:

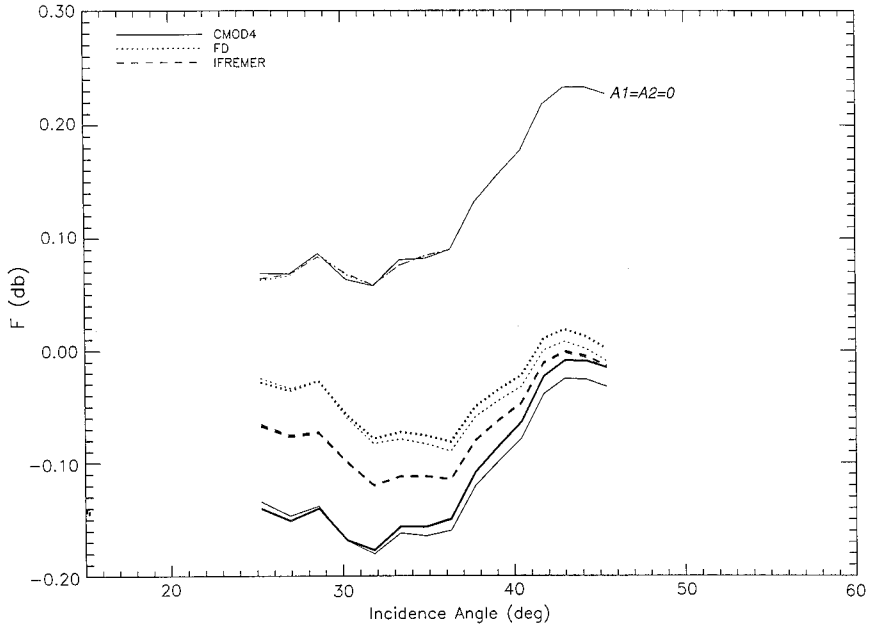

FIG. 9. Antenna calibration error $F(\theta, 2, 3)$ (mid beam relative to aft beam) calculated using various approximations with distributions based on the full 13-month dataset for each model function. Solid lines: CMOD-4 model function; dotted lines: Freilich–Dunbar model function; Dashed lines: IFREMER model function; heavy lines: F calculated using the full expression (10); light unlabeled lines: F calculated using the approximation (11) (i.e., $C_1 = 0$); and light labeled lines: F calculated setting $C_1 = C_2 = 0$.

$$F_{(i,k)}(\theta, b, \hat{b}) = \left(\frac{\langle\hat{\sigma}_o(\theta, b)\rangle_{(i,k)}}{\langle\hat{\sigma}_o(\theta, \hat{b})\rangle_{(i,k)}}\right)\frac{[C_{0,(i,k)}(\theta, \hat{b}) + C_{2,(i,k)}(\theta, \hat{b})]}{[C_{0,(i,k)}(\theta, b) + C_{2,(i,k)}(\theta, b)]}, \quad (13a)$$

where

$$C_{0,(i,k)}(\theta, b) = \int_0^\infty A_0(s; \theta)p_{s,(i,k)}(s; \theta, b)\, ds \quad (13b)$$

and

$$C_{2,(i,k)}(\theta, b) = \int_0^\infty A_2(s; \theta)p_{s,(i,k)}(s; \theta, b)\, ds \times \int_0^{2\pi} p_{\chi,(i,k)}(\chi; \theta, b)\cos(2\chi)\, d\chi. \quad (13c)$$

The CMOD-4 model function was used for the results presented below, although no qualitative differences were found when the other empirical model functions were substituted for CMOD-4.

Mean relative gain error estimates $\langle F(\theta, b, \hat{b})\rangle_k$ calculated by averaging over segments for fixed k are shown in Fig. 11 for $1 \le k \le 8$ and for both mid and fore beams ($\hat{b} = 3$ as in section 5). Notwithstanding the nonlinear dependence of $F_{(i,k)}$ on the sample speed and azimuthal distributions, the mean relative gain error estimates were nearly identical and independent of k for each beam. There is excellent quantitative agreement between the $\langle F(\theta, b, \hat{b})\rangle_k$ estimates and the results of section 5 based on full 56-week sample statistics.

The sample standard deviation of the $F_{(i,k)}$ estimates [denoted $\sigma_F(\theta, k, b, \hat{b})$] is a measure of the variability of the gain error calculated from only a single segment of data (e.g., as would be available in the early portion of a scatterometer mission). Normalized sample standard deviations $[\sigma_F(\theta, k, b, 3)]/\langle F(\theta, b, 3)\rangle_k$ for the mid and the fore beams are shown in Fig. 12 as functions of θ for selected values of k. Calculation of the sample σ_o statistics and velocity distributions from longer data segments generally yields less variable estimates of relative gain errors so that $\sigma_F(\theta, k, b, 3)$ decreases with increasing k. A rapid decrease in normalized standard deviation with increasing k is evident for $k \le 3$ for both the mid and fore beams. Increasing k further did not lead to additional dramatic decreases in $\sigma_F(\theta, k, b, 3)$. It thus seems reasonable to perform initial beam balancing (at least for the *ERS-1* sampling geometry and C-band model function) using as little as 3 weeks of data.

7. Discussion and conclusions

A quantitive technique to determine the relative antenna gain patterns between spaceborne wind scatterometer antennas (beam balancing) using open-ocean backscatter measurements has been developed and tested. Since the ocean is not an isotropic and homogeneous

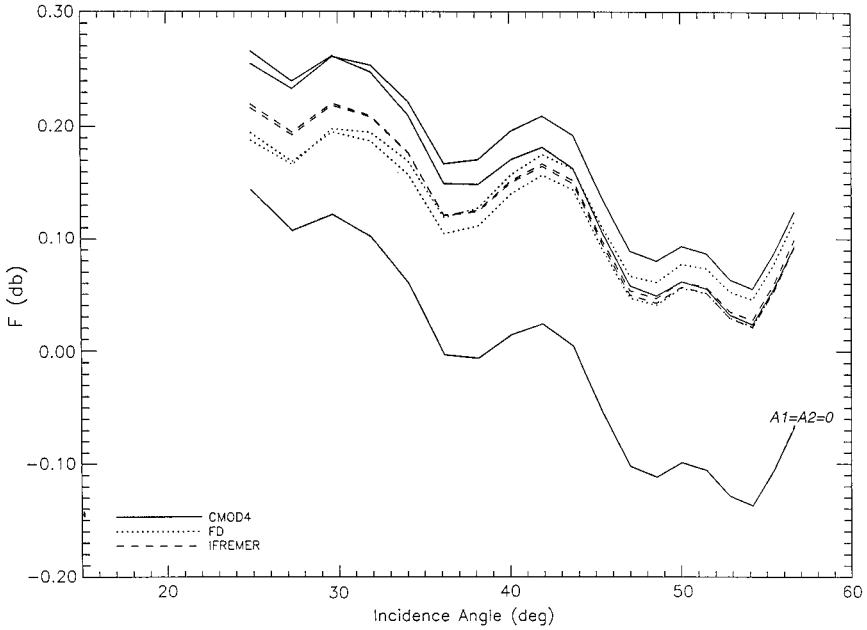

FIG. 10. As in Fig. 9 for $F(\theta, 1, 3)$ (fore beam relative to aft beam).

scatterer, the use of ocean backscatter data for beam balancing requires auxiliary information on the model function and the wind velocity distribution to complement the global ocean mean backscatter values. The analytical development of the technique (primarily described in sections 2 and 4) clearly demonstrates the role played by the auxiliary information and allows examination of the sensitivity of the method to uncertainties in the model function and wind distribution estimates. The technique was tested using *ERS-1* scatterometer measurements from the period 1 June 1992–30 June 1993, several empirical model functions, and wind

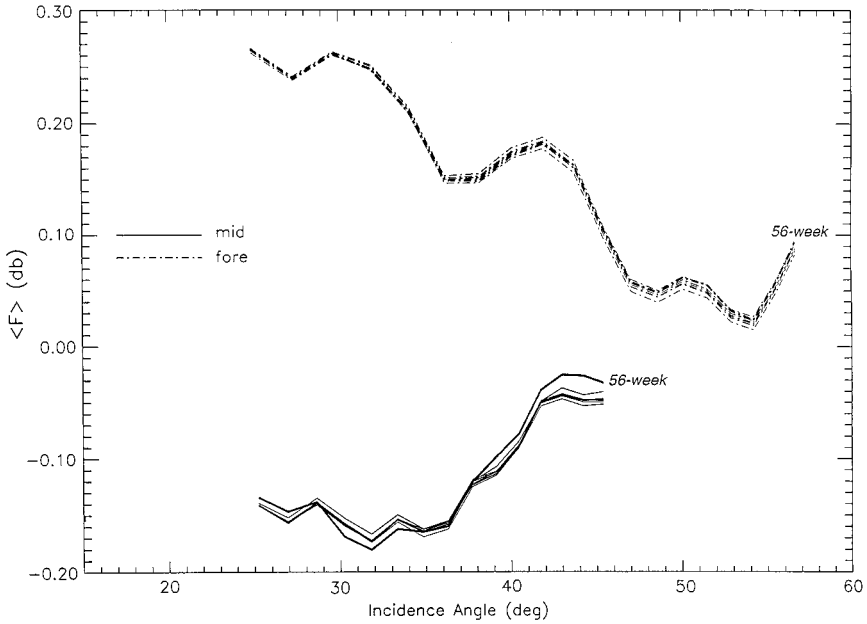

FIG. 11. Mean relative gain error estimates $\langle F(\theta, b, 3)\rangle_\kappa$ for $1 \leq \kappa \leq 8$, where κ denotes the segment length in weeks. Solid lines: $\langle F(\theta, 2, 3)\rangle_\kappa$ (mid beam relative to aft beam); dashed lines: $\langle F(\theta, 1, 3)\rangle_\kappa$ (fore beam relative to aft beam). As the maximum difference between like lines is less than 0.02 dB for $1 \leq \kappa \leq 8$, the κ values corresponding to each line are are omitted for clarity. The CMOD-4 model function was used for all calculations.

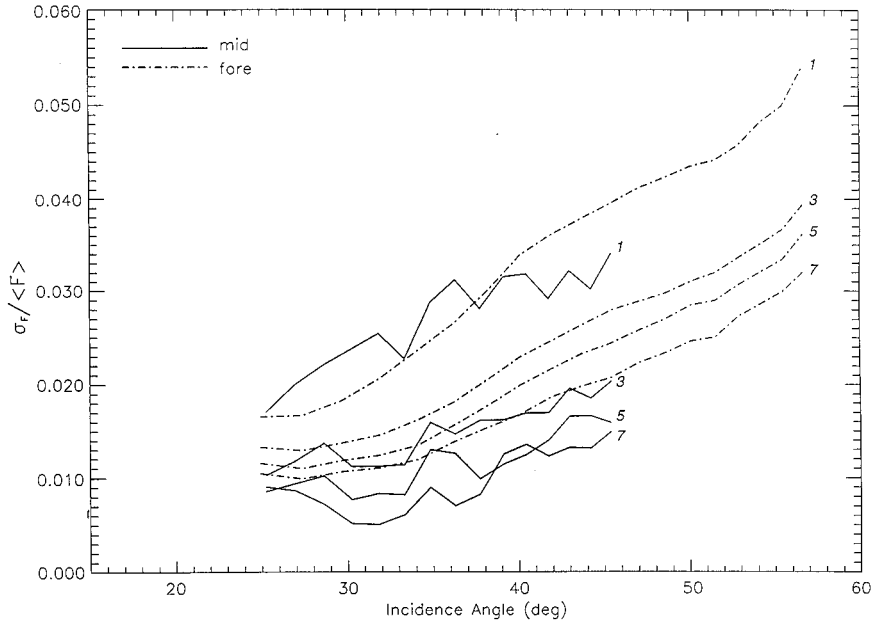

FIG. 12. Normalized sample standard deviations $(\sigma_F(\theta, \kappa, b, 3))/\langle F(\theta, b, 3)\rangle_\kappa$ for the mid and aft beams for selected values of κ calculated using the CMOD-4 model function. Line types as in Fig. 11.

velocity distributions derived from ECMWF and NMC surface wind analyses.

As developed in sections 2 and 4, the technique is sensitive to weighted mean Fourier coefficients of the model function, where the weighting is defined by the distribution of wind speeds imaged by each antenna at each incidence angle. Three different empirical C-band model functions were used in the present study: a truncated azimuthal Fourier series approximation to the CMOD-4 model (Stoffelen and Anderson 1993, 1997a–c; Offiler 1994) used in the European Space Agency's operational processing system; the IFREMER model (Bentamy et al. 1994) based primarily on comparisons between scatterometer and meteorological buoys; and the Freilich and Dunbar (1993b) model based on collocations with operational surface wind analyses (from a different time period than examined in the present beam balancing study). All three model functions had nearly identical weighted means for the lowest (direction independent) coefficient, the mean upwind–downwind $[C_{11}(\theta)]$ coefficients were found to be negligible, and the mean upwind–crosswind coefficients $[C_{21}(\theta)]$ were similar, although not identical, for the three model functions. It was shown both analytically (section 4) and empirically (section 5) that the antenna gain error estimates were relatively insensitive to realistic variations in $C_{21}(\theta)$. All three model functions thus yielded quantitatively similar antenna gain error estimates.

Operational surface wind velocity analyses from ECMWF and NMC were interpolated to the space–time positions of *ERS-1* backscatter measurements to provide estimates of the distributions of wind speed s and relative wind direction χ imaged by each scatterometer antennas at each incidence angle. Using the 56-week dataset, it was shown that the joint distribution $p(s, \chi; \theta, b)$ could be reasonably approximated by the product of a (beam and incidence angle independent) wind speed distribution $p_s(s)$ and an incidence angle-independent azimuthal distribution $p_\chi(\chi; b)$. Further examination in section 3 showed that the 56-week distributions were consistent with ''climatological'' winds dominated by easterly and westerly bands sampled by the near–polar orbiting scatterometer antennas. The separability of the joint distribution into the product of a speed and a directional distribution led directly to significant analytical simplifications.

The wind velocity distribution results have implications for both model function development and future beam-balancing analyses using annual (and longer) scatterometer datasets. A number of authors (e.g., Wentz et al. 1984; Freilich and Dunbar 1993a,b; Freilich and Challenor 1994) have used a Rayleigh distribution to approximate the global ocean wind speeds observed by spaceborne instruments. This approximation is consistent with the wind speed distribution (Fig. 4a) obtained in the present study. However, the model function development approach of Wentz et al. (1984) assumed a uniform relative directional distribution imaged by each scatterometer antenna. Assuming a uniform directional distribution would further simplify the beam-balancing approach (since then $C_{12} = C_{22} = 0$), but, as shown by Fig. 4b, the actual χ distributions are not consistent with uniformity.

The full 56-week dataset was used in section 5 to

estimate antenna gain errors for *ERS-1* and to demonstrate the sensitivity of the technique to various assumptions. Taking the aft beam as the standard, it was shown that the fore-beam gain error was small but positive (in decibels), while the midbeam gain error was even smaller and negative (in decibels). For both beams and all three model functions, the apparent beam imbalance was generally less than 0.2 dB, well within the prelaunch requirements of 0.28 dB (Lecomte and Attema 1993). Both the signs and the magnitudes of the gain errors derived using the open-ocean technique are consistent with those calculated independently by others (e.g., Lecomte and Attema 1993; Long and Skouson 1996; Stoffelen 1999).

Initial postlaunch calibration of scatterometers must be done using data spanning only a few weeks. Section 6 thus empirically examined the sensitivity of the open-ocean beam-balancing technique to the temporal extent of the data used to calculate the sample mean backscatters and wind velocity distribution estimates. It was shown that gain error estimates from 3-week (or longer) data segments had normalized standard deviations less than 4% (0.17 dB). The present method thus holds great promise for both initial beam-balancing analyses using small quantities of data and subsequent precise antenna gain error corrections using annual or longer datasets. As the open-ocean method requires no investment in expensive ground monitoring stations or field campaigns to elucidate the scattering characteristics of vegetation or remote land areas, it should be seriously considered for use in calibrating future fan-beam scatterometers.

Acknowledgments. The *ERS-1* scatterometer backscatter data were kindly provided by the European Space Agency and reformatted and distributed by the Physical Oceanography DAAC at JPL. Ad Stoffelen, David Offiler, David Long, Linwood Jones, and Wu-Yang Tsai made helpful comments during the course of this research. This work was supported in part by the NASA Physical Oceanography Program through Grants NAGW-3062 and NAGW-3615 to Oregon State University and by the JPL NSCAT Project through Contract 959351. Portions of these analyses were performed at the Jet Propulsion Laboratory, California Institute of Technology, under contract with the National Aeronautics and Space Administration.

REFERENCES

Attema, E. P. W., 1991: The active microwave instrument on board the *ERS-1* satellite. *Proc. Inst. Electr. Eng.*, **79,** 791–799.

Bentamy, A., Y. Quilfen, P. Queffeulou, and A. Cavanie, 1994: Calibration of the *ERS-1* scatterometer C-band model. IFREMER Tech. Rep. DRO/OS-94-01, 72 pp. [Available from Institute Français de Recherche pour l'Exploitation de la Mer, B.P. 70, 29280 Plouzane, France.]

Birrer, I. J., E. M. Bracalante, G. J. Dome, J. Sweet, and G. Berthold, 1982: σ_o signature of the Amazon rain forest obtained from the Seasat scatterometer. *IEEE Trans. Geosci. Remote Sens.*, **20,** 11–17.

Freilich, M. H., and R. S. Dunbar, 1993a: Derivation of satellite wind model functions using operational surface wind analyses: An altimeter example. *J. Geophys. Res.*, **98,** 14 633–14 649.

——, and ——, 1993b: A preliminary C-band scatterometer model function for the *ERS-1* AMI instrument. *Proc. First ERS-1 Symp.—Space at the Service of Our Environment,* Cannes, France, European Space Agency, 79–84.

——, and P. G. Challenor, 1994: A new approach for determining fully empirical altimeter wind speed model functions. *J. Geophys. Res.*, **99,** 25 051–25 062.

Kennett, R. G., and F. K. Li, 1989: Seasat over-land scatterometer data, Part II: Selection of extended area land-target sites for the calibration of spaceborne scatterometers. *IEEE Trans. Geosci. Remote Sens.*, **27,** 779–788.

Lecomte, P., and E. P. W. Attema, 1993: Calibration and validation of the *ERS-1* wind scatterometer. *Proc. First ERS-1 Symp.—Space at the Service of Our Environment,* Cannes, France, European Space Agency, 19–29.

Long, D. G., and G. B. Skouson, 1996: Calibration of spaceborne scatterometer using tropical rain forests. *IEEE Trans. Geosci. Remote Sens.*, **34,** 413–424.

Lönnberg, P., D. Shaw, and P. Undén, Eds., 1992: Research manual 1, ECMWF data assimilation, scientific documentation, European Centre for Medium-Range Weather Forecasts, Reading, United Kingdom. [Available from Director, European Centre for Medium-Range Weather Forecasts, Shinfield Park, Reading, Berkshire RG2 9AX, United Kingdom.]

Naderi, F. M., M. H. Freilich, and D. G. Long, 1991: Spaceborne radar measurement of wind velocity over the ocean—An overview of the NSCAT scatterometer system. *Proc. Inst. Electr. Eng.*, **79,** 850–866.

Offiler, D., 1994: The calibration of *ERS-1* satellite scatterometer winds. *J. Atmos. Oceanic Technol.*, **11,** 1002–1017.

Shaw, D. B., P. Lonnberg, A. Hollingsworth, and P. Unden, 1987: Data assimilation: The 1984/1985 revisions of the ECMWF mass and wind analysis. *Quart. J. Roy. Meteor. Soc.*, **113,** 533–566.

Stoffelen, A., 1999: A simple method for calibration of a scatterometer over the ocean. *J. Atmos. Oceanic Technol.*, **16,** 276–284.

——, and D. L. T. Anderson, 1993: *ERS-1* scatterometer data characteristics and wind retrieval skill. *Proc. First ERS-1 Symp.—Space at the Service of Our Environment,* Cannes, France, European Space Agency, 55–59.

——, and ——, 1995: The ECMWF contribution to the characterization, interpretation, calibration and validation of *ERS-1* scatterometer backscatter measurements and winds, and their use in numerical weather prediction models. European Space Agency Contractor Report, 92 pp. [Available from Director, European Centre for Medium-Range Weather Forecasts, Shinfield Park, Reading, Berkshire, RG2 9AX, United Kingdom.]

——, and ——, 1997a: Scatterometer data interpretation: Measurement space and inversion. *J. Atmos. Oceanic Technol.*, **14,** 1298–1313.

——, and ——, 1997b: Ambiguity removal and assimilation of scatterometer data. *Quart. J. Roy. Meteor. Soc.*, **123,** 491–518.

——, and ——, 1997c: Scatterometer data interpretation: Estimation and validation of the transfer function CMOD4. *J. Geophys. Res.*, **102,** 5767–5780.

Wentz, F. J., S. Peteherych, and L. A. Thomas, 1984: A model function for ocean radar cross sections at 14.6 GHz. *J. Geophys. Res.*, **89,** 3689–3704.